How to cite: *Angew. Chem. Int. Ed.* **2022,** *61,* e202113833
International Edition: doi.org/10.1002/anie.202113833
German Edition: doi.org/10.1002/ange.202113833

Catalytic Therapy | Hot Paper

A Nanohook-Equipped Bionanocatalyst for Localized Near-Infrared-Enhanced Catalytic Bacterial Disinfection

Xin Fan, Xizheng Wu, Fan Yang, Lei Wang, Kai Ludwig, Lang Ma, Andrej Trampuz, Chong Cheng,* and Rainer Haag**

Abstract: *Novel bionanocatalysts have opened a new era in fighting multidrug-resistant (MDR) bacteria. They can kill bacteria by elevating the level of reactive oxygen species (ROS) in the presence of chemicals like H_2O_2. However, ROSs' ultrashort diffusion distance limit their bactericidal activity. We present a nanohook-equipped bionanocatalyst (Ni@Co-NC) with bacterial binding ability that shows robust ROS-generating capacity under physiological H_2O_2 levels. The Ni@Co-NC's pH-dependent performance confines its effects to the biofilm microenvironment, leaving healthy tissue unaffected. Furthermore, it can generate heat upon NIR laser irradiation, enhancing its catalytic performance while achieving heat ablation against bacteria. With the Ni@Co-NC's synergistic effects, bacterial populations fall by >99.99%. More surprisingly, the mature biofilm shows no recurrence after treatment with the Ni@Co-NC, demonstrating its tremendous potential for treating MDR bacterial related infections.*

Introduction

Infections by multidrug-resistant (MDR) pathogenic bacteria have afflicted millions of people, and worldwide they cause almost one million deaths every year.[1,2] To address this serious threat to global health, numerous chemically engineered functional nanomaterials with potent antibacterial therapeutic effects have emerged as potential substitutes for traditional antibiotics. This new class of nanomaterials, with mechanisms as diverse as reactive oxygen species (ROS) generation, selective ion leaching, and heat ablation effects, represents a new era in nanomedicine.[3–9] In particular, nanomaterials that can mimic oxidoreductases like peroxidase (POD), oxidase (OXD), and catalase (CAT) have sparked increasing interest because they can be used to fine-tune local ROS levels for satisfactory bactericidal outcomes.[10–15] But these oxidoreductase-mimicking nanomaterials, also known as bionanocatalysts, can show undesirable off-target activity during in vivo biofilm treatment, leading to unpredictable toxicity.[16,17] Therefore, the ideal bionanocatalyst will not only deliver strong catalytic-reaction-based therapeutic effects to biofilm-infected sites, but will limit its action to these sites while leaving healthy tissues unaffected. The pursuit of this combination of traits stands as a significant challenge in developing antibacterial bionanocatalysts.

Under the encapsulation of extracellular polymeric substances, the biofilm microenvironment (BME) usually lacks oxygen, resulting in anaerobic glycolysis, ion channel turbulence, and lower pH ($\approx$5.5).[18] To address these highly complex BME conditions, transition metals (iron, cobalt, nickel, manganese, etc.) that exhibit POD-like catalytic reactions are expected to be promising bionanocatalyst

[*] X. Fan, Prof. Dr. R. Haag
Institute for Chemistry and Biochemistry, Freie Universität Berlin, Takustraße 3, 14195 Berlin (Germany)
E-mail: haag@zedat.fu-berlin.de

X. Fan, Dr. L. Wang, Prof. Dr. A. Trampuz
BIH Center for Regenerative Therapies (BCRT)
Charité-Universitätsmedizin Berlin
Corporate Member of Freie-Universität Berlin
Humboldt-Universität zu Berlin
and Berlin Institute of Health (BIH)
Berlin (Germany)
E-mail: andrej.trampuz@charite.de

X. Wu, Prof. Dr. C. Cheng
College of Polymer Science and Engineering
State Key Laboratory of Polymer Materials Engineering, Sichuan University, Chengdu 610064 (China)
E-mail: chong.cheng@scu.edu.cn

F. Yang
Department of Physics, Freie Universität Berlin, Arnimallee 14, 14195 Berlin (Germany)

Dr. L. Wang, Prof. Dr. A. Trampuz
Center for Musculoskeletal Surgery
Charité—Universitätsmedizin Berlin
Corporate Member of Freie Universität Berlin
Humboldt-Universität zu Berlin
and Berlin Institute of Health
Berlin (Germany)

Dr. K. Ludwig
Research Center for Electron Microscopy and Core Facility BioSupraMol
Institute for Chemistry and Biochemistry
Freie Universität Berlin
Fabeckstrasse 36a, 14195 Berlin (Germany)

Prof. Dr. L. Ma
Department of Ultrasound, West China Hospital, Sichuan University, Chengdu 610065 (China)

candidates because they show ROS generation capabilities that are well-matched to BME pH conditions. With their intrinsic POD-like properties, these transition-metal-based bionanocatalysts can produce ROS in a pH-dependent manner without requiring the additional input of oxygen or energy.[19] Despite significant progress in the design and investigation of POD-like bionanocatalysts, many challenges remain in developing bionanocatalysts for in vivo MDR bacteria biofilm eradication. For instance, at physiological H_2O_2 concentrations (50–100 μM), these transition-metals-based bionanocatalysts can hardly generate levels of hydroxyl radicals (•OH, a kind of ROS) that are sufficient for combating biofilm.[18] Moreover, the ultra-short lifetimes (< 200 ns) of •OH radicals produced at the active sites of bionanocatalysts mean that they are likely to be quenched immediately, limiting both diffusion distance and bactericidal efficacy.[20] Therefore, to further enhance bionanocatalytsts' abilities to destroy MDR bacterial biofilm, we must improve their H_2O_2-catalytic activity in BME conditions and shorten the distance between bionanocatalysts and bacteria. To date, no research has simultaneously overcome these two challenges.

Here we present a nanohook-equipped bionanocatalyst with a nickel-cobalt bimetal doping nanostructure (Ni@Co-NC) for localized, near-infrared laser (NIR)-enhanced catalytic bacterial biofilm disinfection. Two properties of this bionanocatalyst enhance its specificity in targeting bacterial biofilm. First, its unique nanohook-equipped structure enables this Ni@Co-NC bionanocatalyst to spontaneously hook onto bacteria and their biofilm, an effect that localizes its catalytic bactericidal effects to the infected area. Meanwhile, its pH-dependent POD-like catalytic performance limits the biocatalytic effects of Ni@Co-NC to the BME; in other words, Ni@Co-NC catalyzes H_2O_2 to toxic •OH in BME pH conditions while showing no such POD-like •OH generation under physiological neutral pH. Notably, Ni@Co-NC generates heat upon NIR laser irradiation, simultaneously enhancing its catalytic performance and achieving heat ablation against bacteria. As a result of these synergistic effects, bacteria are reduced by over 99.99 % in the presence of Ni@Co-NC. More surprisingly, mature biofilm, whether established in vitro or in vivo, shows no recurrence after treatment with Ni@Co-NC. We propose this new bionanocatalyst forward as a potential candidate for the next generation of antibiotic-free antibacterial strategies to counter MDR bacteria.

Results and Discussion

We began by preparing the nanohook-equipped bionanocatalyst, Ni@Co-NC, via the pyrolysis of a Ni-doped zeolitic imidazolate framework-67 (ZIF67), termed as Ni@ZIF67 and illustrated in Figure 1a. For comparison in the further structural and catalytic study, we also produced its cousin material Co-NC by the same protocol, except without the addition of nickel. We then systematically studied the chemical and physical structures of Ni@Co-NC by scanning electron microscopy (SEM), transmission electron microscopy (TEM), X-ray diffraction (XRD), X-ray photoelectron spectroscopy (XPS), and X-ray absorption energy near-edge structure (XANES). Both TEM images (Figure 1b and Figure 1c) and SEM images (Figure S1) confirmed that the carbon nanotubes (CNTs) could be generated by adding an extra amount of dicyandiamide (DCD) during the carbonization process of Ni@Co-NC. The DCD decomposed and generated ammonia gas and acted as carbon and nitrogen sources for the generation of CNTs; the morphologies of Ni@Co-NC synthesized with the different amounts of DCD are shown in Figure S2 (detailed mechanism was discussed in the synthesis part in the Supporting Information). These carbon nanotubes can function as nanohooks to interact with bacteria and biofilm, as we will demonstrate below after a brief material characterization of Ni@Co-NC. The XRD pattern of Ni@Co-NC (Figure S3) shows five peaks located at 26.0°, 36.8°, 44.3°, 51.5°, and 76.0°, corresponding respectively to the (002) facet of the graphite layer, the (311) facet of cobalt oxide, while the (111), (200), and (220) facets of face-centered cubic (FCC) Co and Co–Ni alloy metals. The selected area electron diffraction (SAED) (Figure 1d) indicated the major diffraction rings of the Ni@Co-NC, which matches well with the XRD data. Energy-dispersive spectroscopy (EDS) mapping (Figure 1e) also revealed that C, N, Co, and Ni elements were homogeneously distributed throughout the Ni@Co-NC.

To further verify and quantify the atomic Co and Ni distribution in the CNTs' structures, we conducted STEM-based line scanning across the nanocrystal (Figure 1f). Site I, at a distance of around 5 nm, showed a high C signal but low and uniform Co, Ni, and N signals, reflecting the carbon layer with Co-N_x and Ni-N_x sites; while site II, at a distance of around 14 nm, displayed an element ratio, for C:N:Co:Ni, of 10.54:1:36.18:1.06, suggesting the coexistence of Ni-N_x sites and Co nanoparticles. High-resolution TEM images of the end of the nanohook (Figure 1g) showed the lattice fringes of both carbon layers and nanocrystalline Co and Co–Ni alloys, wherein 0.325 nm reflects the typical interlayer d-spacing of C (002) and 0.198 nm is the d-spacing of the Co and Co–Ni alloys' (111) planes. We used XPS to analyze the chemical composition, binding states, and atomic ratio of Ni@Co-NC (Figure S4). Taken together, these results demonstrate the unique structure of Ni@Co-NC, whose surface is equipped with nanohooks consisting of abundant Co-N_x, Ni-N_x, and cobalt nanoparticles sites.

To understand the influence of Ni incorporation on the local structure of Co sites within Ni@Co-NC, we performed XANES spectroscopy. As a reference, we also plotted Co foil, CoO, Co_3O_4, and Co-NC. Co K-edge XANES data (Figure 1h) revealed Ni@Co-NC and Co-NC showed similar position and intensity of Co pre-edge, indicating that Ni ions homogeneously replace Co sites of ZIF67 without changing the coordination geometry.[21]

According to previous studies, the oxidation states of catalytic centers can greatly affect their structures and properties, such as spin state and work function. Thus, by regulating the oxidation states, the catalytic performance of the catalytic center can be improved.[22] The absorption energies of both Ni@Co-NC and Co-NC fall between those

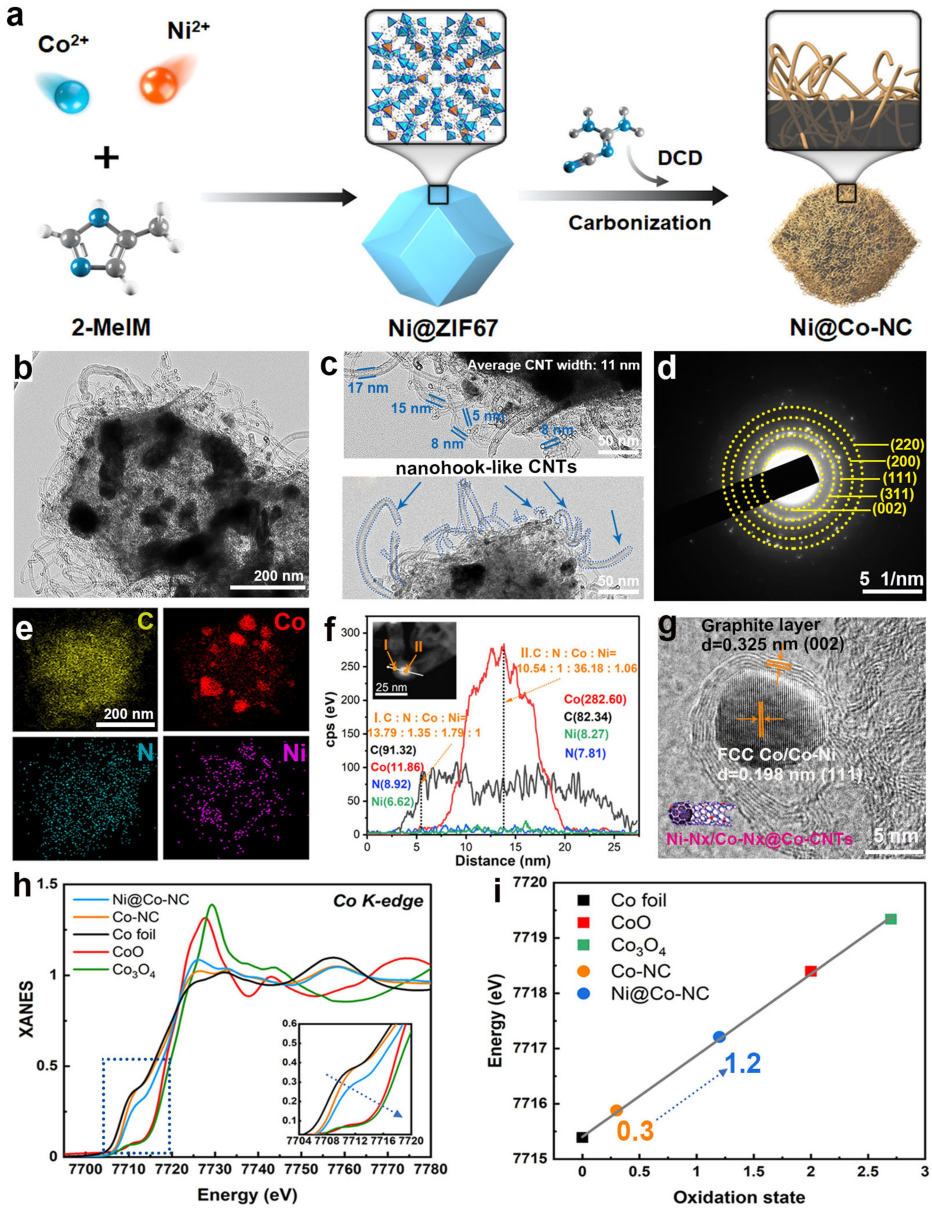

Figure 1. Fabrication of Ni@Co-NC, and its morphological and structural characterizations. a) Scheme of synthesis of Ni@Co-NC. b, c) TEM images reveal the unique nanohook-equipped structure of Ni@Co-NC. d) Selected area electron diffraction (SAED) pattern and e) EDS mapping of Ni@Co-NC. f) STEM images and corresponding elemental line scan of Ni@Co-NC, showing nanohook with Co nanoparticles and Co-N_x and Ni-N_x sites. g) High-resolution TEM image, h) XANES, and i) oxidation state analysis of Ni@Co-NC.

of Co foil and CoO, indicating that their cobalt sites show oxidation states between 0 and 2. In light of the standard curve fitted by reference compounds with known oxidation states,[23] we were surprised to find that after introducing a trace amount of Ni species at a Ni:Co doping molar ratio of 1:40, the average oxidation state of cobalt increased significantly from 0.3 to 1.2 (Figure 1i), indicating that the interaction between Co and Ni within Ni@Co-NC may have caused an electron transfer from Co to Ni, thus increasing the oxidation state of Co.[24]

Transition metal doping is a good strategy for modulating the d-band center of catalytic sites, thus optimizing the catalytic process.[25–27] Based on this knowledge, combined with the ability of oxidation state regulation to improve catalytic function, we anticipated that the oxidation state enhancement of the catalytic center, caused by doping with trace amounts of nickel, would further affect the POD-like catalytic performance of the cobalt center.

Therefore, to understand whether nickel doping promoted the POD-like performance of Co-NC, we examined hydroxyl radicals •OH, the representative bactericidal product of the POD-like reaction, in the presence of H_2O_2. At a BME pH of ≈5.5, Ni@Co-NC generated a significantly larger amount of •OH than Co-NC, implying that the nickel doping promoted the POD-like catalytic performance (Figure 2a). Also, we noticed that Ni@Co-NC showed the best

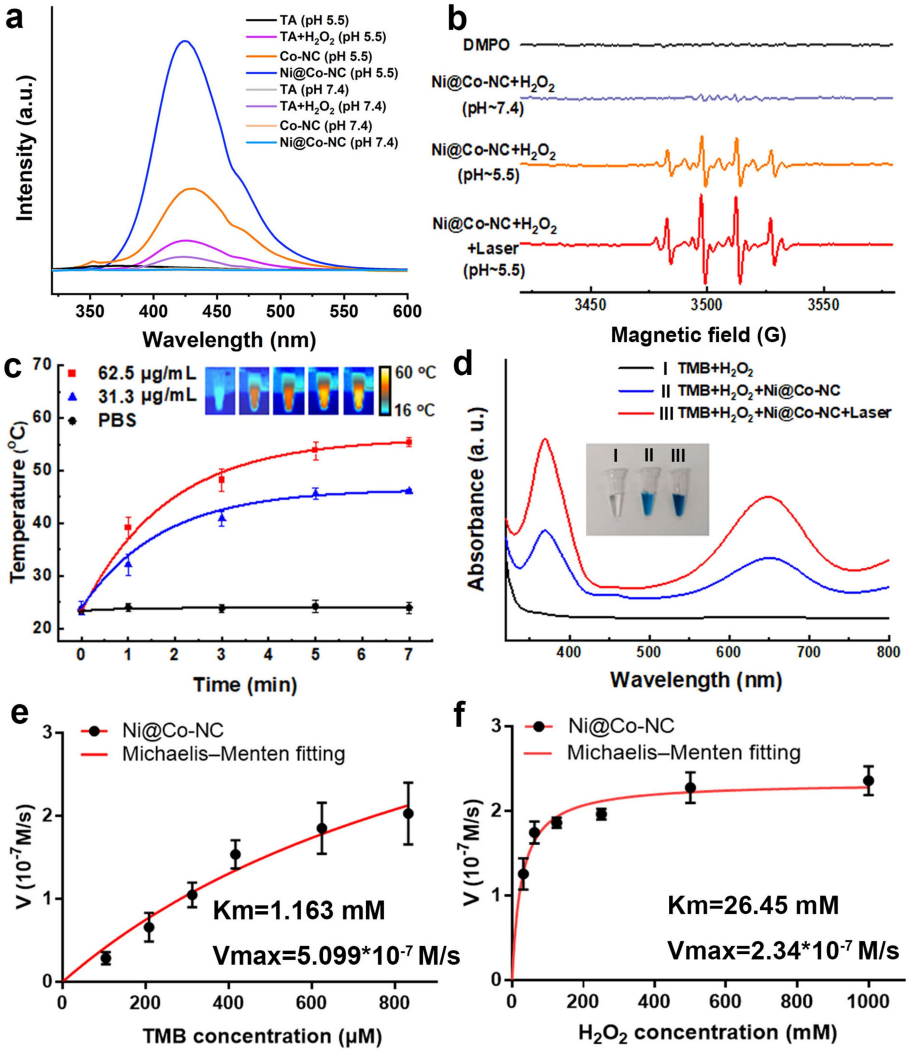

Figure 2. pH-dependent NIR-enhanced catalytic performance of Ni@Co-NC. a) Ni@Co-NC's •OH generation ability at biofilm microenvironment pH (5.5) and physiological pH (7.4) in the presence of H_2O_2. Both Co-NC and Ni@Co-NC groups contained 3 mM of terephthalic acid and 100 μM of H_2O_2. b) ESR data reveal the NIR-enhanced •OH generation. c) Photothermal heating profile of Ni@Co-NC exposed to NIR laser at a power density of 1 $W cm^{-2}$. Inset: infrared photos of Ni@Co-NC solution (62.5 $\mu g mL^{-1}$) exposed to laser for 0, 1, 3, 5, and 7 min. d) NIR-enhanced POD-like activity of Ni@Co-NC. Steady-state kinetic assay of Ni@Co-NC for TMB (e) and H_2O_2 (f).

•OH generation ability compared to its related nanomaterials synthesized with different pyrolysis temperatures (Figure S5), while we saw nearly no •OH generation at a physiological pH of ≈7.4, suggesting that pH can serve as a switch for the POD-like ROS generation behavior of Ni@Co-NC. Interestingly, we noticed that the POD-like ROS generation was further enhanced by exposing Ni@Co-NC to NIR laser radiation, a result that was confirmed by electronic spin resonance (ESR). Characteristic ESR signals of 5,5-dimethyl-1-pyrroline N-oxide (DMPO)-OH with an amplitude ratio of 1:2:2:1 were clearly observed in an acidic environment and were intensified upon introducing NIR radiation, elucidating the bionanocatalyst's NIR-enhanced POD-like potential (Figure 2b). According to the Arrhenius equation,[28,29] the chemical reaction can be significantly accelerated by increasing temperature; therefore, by comparing the POD-like activity of Ni@Co-NC under four different conditions, we found the NIR-enhanced POD-like activity can be attributed to the temperature rising owing to photothermal conversion property of Ni@Co-NC (Figure S6a). We further monitored the NIR-induced heating profile of Ni@Co-NC. The Ni@Co-NC showed a concentration-dependent temperature increase after exposure to NIR laser (Figure 2c). We observed that the temperature rose to 55.4 °C within 7 minutes at a concentration of 62.5 $\mu g mL^{-1}$, while we observed no significant temperature variation for the PBS, confirming the robust photothermal conversion ability of Ni@Co-NC. Interestingly, we found that this unique nanohooks-equipped structure promote the photothermal properties (Figures S6b, S7a, and S7c, detailed discussion is presented in the Supporting Information). Moreover, the dispersity of the Ni@Co-NC with different concentrations under biological media was examined (Figure S8).

We then selected the most common and sensitive POD substrate, 3,3′,5,5′-Tetramethylbenzidine (TMB), to test the POD-like activity and steady-state kinetic parameters of Ni@Co-NC. After a 5-min incubation, the TMB + H_2O_2 + Ni@Co-NC group exhibited blue products with remarkable absorption peaks reflecting oxidized TMB at both 370 nm and 652 nm, revealing robust POD-like activity (Figure 2d). Meanwhile, this POD-like activity was also strengthened upon NIR laser activation. We noticed the production of dark blue products with intensified absorption peaks for the laser-exposed group, resulting from the promotion of TMB oxidation by NIR-enhanced •OH generation. The dose-dependent POD-like activity of Ni@Co-NC was exhibited in Figure S6c. Moreover, we calculated the Michaelis–Menten constant (K_m) and the maximum initial velocity (V_{max}) to assess the catalytic performance of Ni@Co-NC (Figures 2e,f and Table S1). The K_m value of the Ni@Co-NC was 26.45 mM for H_2O_2 substrate and 1.163 mM for TMB substrate, indicating the comparable affinity of Ni@Co-NC for H_2O_2 and TMB substrates with that of natural horseradish peroxidase (HRP) (3.70 mM for H_2O_2 substrate and 0.434 mM for TMB substrate). Meanwhile, by comparing the K_m values of Ni@Co-NC (26.45 mM) and Co-NC (41.64 mM) (Figure S9), we noticed that the affinity between the bionanocatalyst and H_2O_2 substrate was significantly enhanced after nickel doping.[30] Importantly, the V_{max} values of Ni@Co-NC for H_2O_2 and TMB showed respective ≈1.2-fold and ≈2-fold increases relative to Co-NC, suggesting that the nickel doping accelerated the POD-like catalytic process. Furthermore, by comparing with the nanohook-free sample, Ni@ZIF67-C, we found that the anchoring of nanohooks could also enhance the POD-like activity of the materials by enriching the superficial N-doped carbons and metal-N_x sites, which have also been observed by previous studies (Figures S6d,e, S7b,d, detailed discussion is presented in the Supporting Information).[31,32] The above experimental results confirm that both Ni doping and anchoring of nanohook can promote the POD-like activity; meanwhile, the Ni@Co-NC offers NIR-enhanced and pH-selective POD-like performance, thus giving it tremendous potential for achieving on-demand BME-targeted catalytic disinfection.

Next, to study the possible in vitro planktonic MRSA killing actions of Ni@Co-NC, we used confocal laser scanning microscopy (CLSM), cryogenic electron microscopy (cryo-EM), and SEM to observe the interactions between Ni@Co-NC and MRSA. First, we used CLSM to investigate MRSA (stained by fluorescein isothiocyanate, or FITC) and treated with Ni@Co-NC (non-covalently labeled by rhodamine B) for different incubation times (Figure S10). We noticed that Ni@Co-NC gradually bound with the bacteria cells as the incubation time increased, and we detected a higher intensity of bacteria cells with fluorescence; meanwhile, from colocalization analysis, after 30 min of incubation, the Pearson's correlation coefficient reached 0.5183, revealing the high colocalization relation between Ni@Co-NC and MRSA and thus indicating that Ni@Co-NC had bonded to the MRSA cell surface. SEM images showed that the amount of Ni@Co-NC bonded to the MRSA cell surface was remarkably higher than the nanohook-free sample, Ni@ZIF67-C, thus demonstrating that the nanohooks did facilitate the bacterial binding ability of bionanocatalysts (Figure S11). Meanwhile, SEM and TEM images offered a close-up depiction of the binding between Ni@Co-NC and MRSA via nanohooks (Figure S12).

We further carried out cryo-EM measurements to monitor the actions of Ni@Co-NC against MRSA. For untreated MRSA, cryo-EM images confirm its intact dual-membrane morphology (Figure 3b). However, after treating the MRSA with Ni@Co-NC, we observed Ni@Co-NC hooking onto the MRSA surface (Figure 3c, orange arrows), facilitated by its nanohook-equipped structure. To prove direct hooking of the Ni@Co-NC to the bacterium, which is difficult to determine from individual projection images alone, we also recorded side-by-side stereograms (stereo pairs of cryo-EM at 8° view angle) (Figure S13). The introduction of laser and H_2O_2 activated the bactericidal potential of Ni@Co-NC. We observed that the deformed MRSA cells suffered from severe membrane disruption or that the bacteria retained only part of their transparent outer membrane structure and underwent significant cytoplasm leakage. These results indicate the violent bactericidal actions of localized ROS and photothermal ablation caused by Ni@Co-NC (Figures 3d and S14). The protein leakage profile (Figure 3e) also provides strong evidence of disrupted MRSA membrane structure and cytoplasm leakage. As a result, MRSA treated with activated Ni@Co-NC (a term we use to refer to Ni@Co-NC activated by both laser and H_2O_2 unless otherwise stated) showed remarkably higher protein leakage amount than other groups treated under different conditions. This higher leakage suggests that the NIR-enhanced ROS generation and ablation effects promoted the protein leakage, an effect that we ascribe to the unmatched severity of bacterial membrane structural damage that we observed under treatment with activated Ni@Co-NC.

To investigate the bactericidal efficacy of Ni@Co-NC in mildly acidic environments, we calculated the bactericidal ratio by agar plate counting (Figures 3f and S15). We observed a bactericidal ratio of over 99.99 % at a concentration of 62.5 μg mL^{-1} of activated Ni@Co-NC, whereas we witnessed a much weaker bactericidal efficacy for the nanohook-free sample (Ni@ZIF67-C) at the same condition, indicating that the nanohooks can induce both binding ability and promote the bactericidal efficacy (Figure S16a). At this concentration, we also found significant bacterial viability reduction for the H_2O_2-activated Ni@Co-NC treatment group, with a bactericidal ratio of 89.95 %. In contrast, we saw poor bactericidal effects for Ni@Co-NC + laser and bare Ni@Co-NC groups, with respective bactericidal ratios of 36.16 % and 10.21 %. Therefore, the H_2O_2 activation should be regarded as a major contributor to the bactericidal performance, and the laser activation function as a coadjutor that further promotes bactericidal outcomes via ablation and acceleration of ROS generation. Also, this bactericidal action was effective towards gram-negative drug-resistant bacteria (Figure S17). It is worth mentioning that negligible

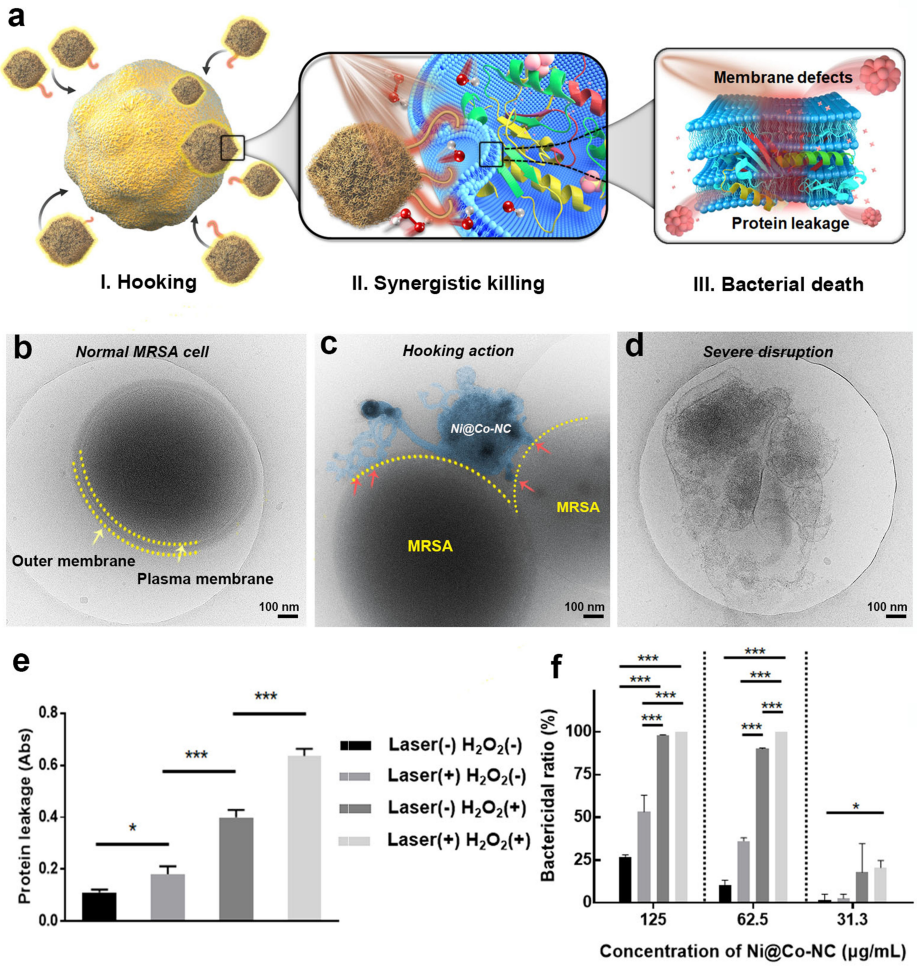

Figure 3. In vitro planktonic MRSA killing profile of Ni@Co-NC. a) This schematic image shows that Ni@Co-NC can hook onto bacterial surfaces and kill them through localized NIR-enhanced ROS generation and heat ablation, resulting in severe membrane disruption and intracellular substance leakage. Cryo-EM images of b) normal MRSA cell, c) MRSA cells incubated with Ni@Co-NC for 30 min, and d) disrupted MRSA cell treated with NIR-activated Ni@Co-NC and H_2O_2. e) Bacterial protein leakage profile and f) bactericidal ratio of Ni@Co-NC under different activation conditions. All experimental data are displayed as the average values (mean ± SD, $n = 3$). Asterisks indicate significant differences ($^*P < 0.1$, $^{**}P < 0.01$, $^{***}P < 0.001$).

bactericidal activity was found for activated Ni@Co-NC (62.5 $\mu g\,mL^{-1}$) in the neutral environment, implying moderate behavior by Ni@Co-NC in physiological conditions (Figure S16b). Together these results show that Ni@Co-NC can first bind to the bacterial surface through hooking action and then synergistically kill bacteria through localized NIR-enhanced ROS generation and heat ablation, resulting in severe membrane disruption and intracellular substance leakage (Figure 3a).

Encouraged by the bionanocatalyst's robust planktonic MRSA killing performance, we then tested Ni@Co-NC for mature biofilm eradication. We first investigated the biofilm binding ability of Ni@Co-NC with CLSM. Due to the strong bionanocatalyst–bacteria interaction that we demonstrated above, the dye-labeled Ni@Co-NC could also bind accurately to the biofilm area after a 30-min incubation, providing strong support for subsequent biofilm eradication (Figure S18). Next, the biofilms treated with Ni@Co-NC under different activation conditions were stained with a live/dead BacLight bacterial viability kit and observed using 3D CLSM (Figures 4a and 4b). Compared with untreated MRSA biofilm, the biofilms' viability under Ni@Co-NC or Ni@Co-NC + laser treatments showed a very slight decrease, indicating biofilms' powerful barrier effects against heat and foreign substances. Notably, for biofilms treated with Ni@Co-NC + H_2O_2, live (green) signals become very weak and sparse, with a viability of 32.26 %. This result suggests that a great deal of biofilm can be killedvia the localized ROS generation catalyzed by Ni@Co-NC. Strikingly, the biofilms treated with Ni@Co-NC + laser + H_2O_2 showed conspicuous red fluorescence, while green fluorescence was nearly non-detectable due to the strong synergistic actions of NIR-enhanced ROS generation and heat ablation. Furthermore, to study whether biofilm would recur after treatment, we used an isothermal microcalorimetry instrument that can non-destructively monitor the heat flow related to microbial metabolism to detect the growth of biofilm for another 48 h after treatment (Figure 4c). Com-

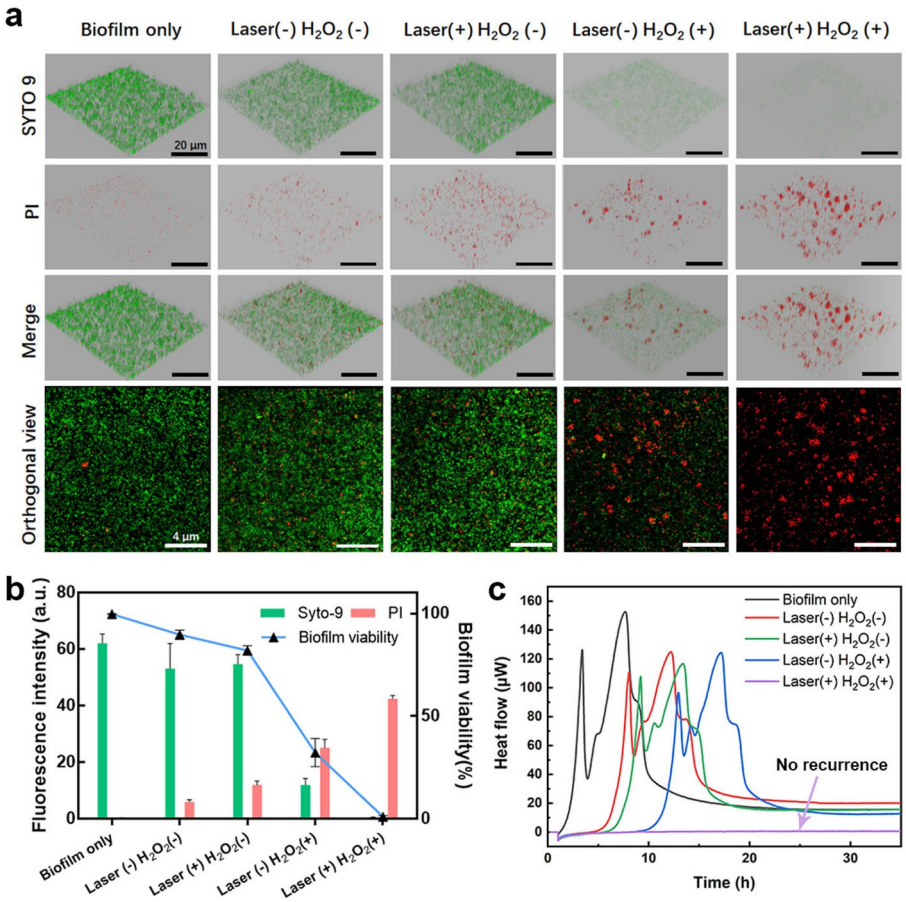

Figure 4. Antibiofilm profile of Ni@Co-NC. a) CLSM images of MRSA biofilm after incubation with PBS and Ni@Co-NC under different activation conditions (green fluorescence: live MRSA biofilm stained with SYTO 9; red fluorescence: dead MRSA biofilm stained with propidium iodide (PI)). Black scale bar is 20 μm; white scale bar is 4 μm. b) Semiquantitative statistics of biofilm viability from analysis of fluorescence intensity percent of SYTO 9 over total fluorescence intensity of SYTO 9 and PI. c) Microcalorimetry analysis of MRSA biofilm after different treatments. Each curve shows the heat produced by viable bacteria within biofilm after treatment under different conditions.

pared to untreated biofilm, we saw different levels of heat flow production delays in biofilms treated with Ni@Co-NC, Ni@Co-NC + laser, and Ni@Co-NC + H_2O_2, indicating that these treatments can somewhat reduce the number of viable cells within the biofilm and delay biofilm recurrence, while still struggling to achieve complete biofilm eradication. By contrast, no heat flow production was seen in the Ni@Co-NC + laser + H_2O_2 treated group, demonstrating that the activated Ni@Co-NC could inflict irreversible damage on biofilms and thoroughly eradicate them. In this way, we showed that activated Ni@Co-NC could easily bind with bacteria and biofilm and achieve striking bactericidal activity via localized NIR-enhanced ROS generation and heat ablation.

Before performing animal experiments, we investigated the cytotoxicity of Ni@Co-NC using human skin keratinocytes (Figure S19). The results confirmed a very low toxicity of Ni@Co-NC under effective bactericidal concentration (90.7 % cell viability under 62.5 $\mu g\,mL^{-1}$). We performed a wound disinfection experiment to further verify the feasibility of Ni@Co-NC as an in vivo biofilm treatment. We first established the biofilm infected wounds on rabbits' epidermis by removing an area of skin 1 cm in diameter and introducing MRSA (dosage: 100 μL; concentration: 1×10^8 CFU mL^{-1}). One day after introducing bacteria, we observed a heavily infected wound with abscess, and then we applied the activated Ni@Co-NC for short-term treatment. After treatment, the pyogenic wound recovered quickly with epidermal tissue regeneration (Figure 5a).

In these animal experiments, to evaluate the in vivo antibiofilm efficacy of activated Ni@Co-NC, we used H_2O_2, Ni@Co-NC + laser, and Ni@Co-NC + H_2O_2 as comparisons. We also tested vancomycin in view of its role as the typical clinical strategy against MRSA. We used a digital camera to record the entire process of wound healing (Figures 5b and S20). The image made clear that after being infected with MRSA for 1 day, the wounds formed abscesses full of sanies, demonstrating MRSA colonization and biofilm formation. On day 2 we performed different treatments and used a thermal imaging camera to monitor the in vivo NIR-triggered heating profile of Ni@Co-NC. Due to the robust photothermal conversion ability of Ni@Co-NC, the temperature rose rapidly to 55 °C after a 2-minute irradiation (2.5 W cm^{-2}), the time is sufficient for the acceleration of

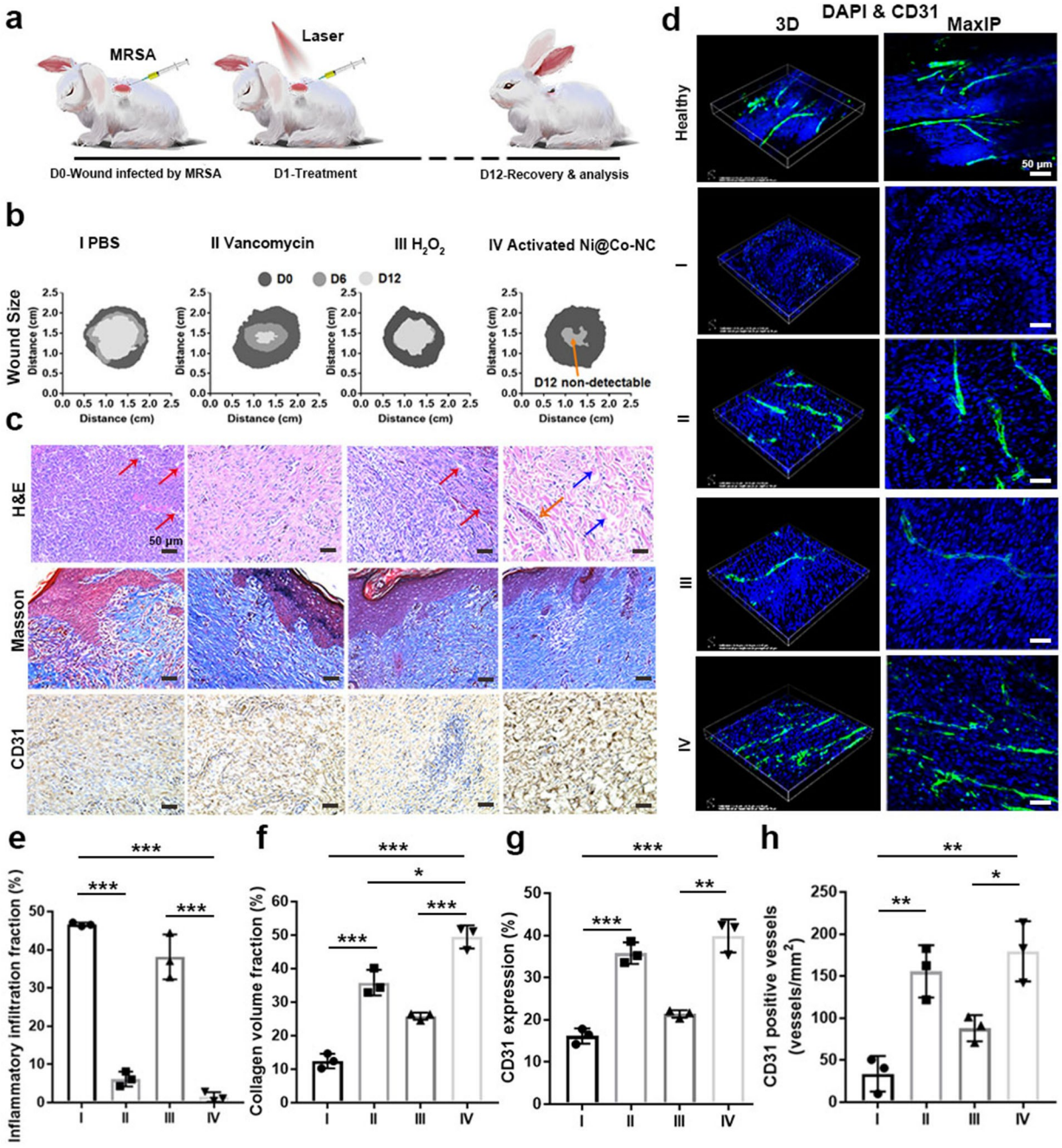

Figure 5. In vivo antibiofilm performance of Ni@Co-NC. a) Schematic illustration of the treatment schedule for in vivo antibiofilm experiment. b) Traces of wound closure over 12 days for groups treated with (I) PBS, (II) vancomycin, (III) H_2O_2, and (IV) Ni@Co-NC + laser + H_2O_2. c) Histologic analysis of the wounds treated by (I)–(IV) after 12 days of therapy. Black scale bar is 50 μm. In this experiment, we used H&E, Masson, and CD31 staining, respectively, to study inflammation response, collagen deposition, and revascularization in the wound area. d) CD31 and DAPI staining images of 3D reconstruction and corresponding maximum intensity projection (MaxIP) for healthy tissue and wounds treated by (I)–(IV). White scale bar is 50 μm. e) Inflammatory infiltration fraction, f) collagen volume fraction, g) CD31 expression, and h) CD31 positive vessels number of wounds treated by (I)–(IV) after 12 days of therapy. Asterisks indicate significant differences ($*P<0.1$, $**P<0.01$, $***P<0.001$). All data were acquired from the rabbits' wound tissues in different groups 12 days after treatment. All values are expressed as mean ± SD, $n=3$.

catalytic procedure as well as bacterial ablation, and will not lead to skin burns (detailed discussion is presented in the Supporting Information). Whereas very limited temperature change was detected for the PBS group (Figure S21). After treatment, we collected bacteria from the wound area and monitored them through agar plate counting (Figure S22). We found no viable bacterial colonies for wounds treated with vancomycin or with activated Ni@Co-NC. These comparable results show that our activated bionanocatalyst achieves highly efficient bactericidal activity on par with

antibiotics. In contrast, numerous viable bacteria remained after the other three treatment groups, suggesting that they offer limited disinfection capabilities. As shown in wound stack diagrams and wound photos (Figures 5b and S20), wounds treated with PBS, H_2O_2, and Ni@Co-NC + laser remained swollen with very limited closure until day 6. By contrast, for wounds treated with either vancomycin or activated Ni@Co-NC, the sanies vanished and we observed apparent area reductions. Notably, by day 12, the activated Ni@Co-NC-treated wound made a full recovery. In the vancomycin-treated group, only very small wounds remained at this time. On the contrary, we saw much slower closures for the groups treated with PBS, H_2O_2, Ni@Co-NC + laser, and Ni@Co-NC + H_2O_2, with large wounds encompassing different levels of the swollen epidermis, indicating an ongoing inflammatory response. To further investigate the infection state of wounds, we also performed the pathological analysis of histological sections via hematoxylin and eosin (H&E) staining. Compared to healthy tissues, we observed large areas of neutrophil infiltration and necrobiotic cells (indicated by red arrows) for PBS, H_2O_2, Ni@Co-NC + laser, and Ni@Co-NC + H_2O_2 groups (Figures 5c and S23), suggesting unrecovered inflammation responses induced by MRSA; meanwhile, the collagen fibrils in the intercellular substance also showed disordered texture, signifying severe damage during infection. We observed that the wounds treated with PBS and H_2O_2 showed very high respective inflammatory infiltration fractions (IIFs) of 46.63 % and 38.13 %. The Ni@Co-NC + laser and Ni@Co-NC + H_2O_2 groups also showed inflammatory response; however, after treatment with vancomycin and activated Ni@Co-NC, their respective IIF values decreased significantly to 6.17 % and 1.47 %, respectively (Figure 5e). Meanwhile, we noted nascent fibroblasts (indicated by blue arrows) and vessels (orange arrows), which confirmed the highly efficient and effective wound disinfection capability of activated Ni@Co-NC. Moreover, we uncovered no apparent rejection reaction or accumulation of Ni@Co-NC in the regenerated epidermis. And more importantly, the wounds treated with activated Ni@Co-NC show similar pathological characteristics to those treated with vancomycin, showing the remarkable potential of the activated Ni@Co-NC system as an antibiotic alternative. Furthermore, we carefully investigated the biosafety of activated Ni@Co-NC via H&E staining of the major organs (Figure S24). The lack of observable lesions confirms the safety of Ni@Co-NC-based NIR-enhanced catalytic therapy. We also performed Masson's trichrome staining to investigate collagen recovery in the wound healing process (Figures 5c, f, and S23). Here the group treated with activated Ni@Co-NC showed extensive and well-organized collagen deposition, with the highest collagen volume fraction of any group (49.48 %).

Neovascularization typically accompanies the wound healing process.[33] With the help of CD31 staining, endothelial cells can be labeled to show newly formed vessels during the recovery of the wound area. As shown in Figures 5c and 5g, small CD31-positive areas were found in the PBS and H_2O_2 groups, with expressions of 16.18 % and 21.39 %. The Ni@Co-NC + laser and Ni@Co-NC + H_2O_2 groups showed increased CD31 expressions (Figure S23), but the groups treated with activated Ni@Co-NC and vancomycin showed even further increased CD31 expressions of 35.81 % and 39.88 %, respectively, thus demonstrating better wound healing outcomes. Furthermore, we used CLSM imagery and immunofluorescence staining of CD31 to create a 3D reconstruction of the revascularization (Figures 5d, h and S25). This reconstruction revealed that the groups treated with activated Ni@Co-NC (179.53 vessels mm^{-2}) and vancomycin (155.82 vessels mm^{-2}) showed the highest number of new capillaries, indicating accelerated wound healing compared to the other groups. Taken together, these results confirm that activated Ni@Co-NC can effectively eradicate bacteria in vivo and achieve accelerated regenerative wound healing.

Conclusion

We have developed a nanohook-equipped bionanocatalyst, Ni@Co-NC, for localized NIR-enhanced catalytic bacterial and biofilm disinfection. With its unique nanohook-equipped structure, this bionanocatalyst can spontaneously hook onto bacteria and biofilms, thus localizing its catalytic bactericidal effect to the site of infection. And because of its pH-dependent catalytic performance, Ni@Co-NC can confine its catalytic activities to biofilm-infected sites while remaining safe to healthy tissue at neutral pH. Notably, upon NIR laser irradiation, Ni@Co-NC can generate heat, which simultaneously enhances its catalytic performance and enables heat ablation against bacteria. As a result of these synergistic effects, bacterial populations are significantly reduced (by >99.99 %) in the presence of Ni@Co-NC. More surprisingly, no recurrence is seen for mature biofilm established either in vitro or in vivo after treatment with Ni@Co-NC. It is believed that this bionanocatalyst will not only be a promising candidate in the next generation of antibiotic-free disinfector against topical or subcutaneous biofilm-related infection but also provide new perspective for the design of bionanocatalytic antimicrobials. Besides, the bionanocatalysts also face some challenges, for example, due to its size and unknown accumulative toxicity in bloodstream and organs, it is yet difficult to be given intravenously and cure unknown bacterial infected lesions as traditional antibiotics do, but we optimistically believe those issues will be solved in the near future, and bionanocatalysts-based antibacterial therapy will achieve unparalleled success.

Acknowledgements

This work was financially supported by the National Key R&D Program of China (2019YFA0110600, 2019YFA0110601), and the Deutsche Forschungsgemeinschaft (DFG) of Germany through grants from Collaborative Research Centers (SFB) 765 and 1449. We also acknowledge the assistance of the Core Facility BioSupraMol supported by the DFG. X. Fan, F. Yang, and L. Wang

acknowledge the support of the China Scholarship Council (CSC). Prof. C. Cheng and Dr. L. Ma are grateful for support from the National Natural Science Foundation of China (Nos. 52173133, 82102064, 82102065, 82071938, 82001824, and 82001829), the Science and Technology Project of Sichuan Province (Nos. 2021YFH0087, 2021YFH0135, 2021YFS0050, 2021YJ0434, 21YYJC2714, 21ZDYF3763, 2021YFH0180, 2020YFH0087, and 2020YJ0055), the 1·3·5 Project for Disciplines of Excellence, West China Hospital, Sichuan University (No. ZYJC21047), the State Key Laboratory of Polymer Materials Engineering (Grant No. sklpme2021-4-02). The authors are grateful for the support of Benjamin Allen in polishing the language of the manuscript. Open Access funding enabled and organized by Projekt DEAL.

Conflict of Interest

The authors declare no conflict of interest.

Keywords: Antibacterial · Biofilm Microenvironment · Bionanocatalysts · Catalytic Therapy · Regenerative Wound Healing

[1] W. Kim, W. Zhu, G. L. Hendricks, D. Van Tyne, A. D. Steele, C. E. Keohane, N. Fricke, A. L. Conery, S. Shen, W. Pan, K. Lee, R. Rajamuthiah, B. B. Fuchs, P. M. Vlahovska, W. M. Wuest, M. S. Gilmore, H. Gao, F. M. Ausubel, E. Mylonakis, *Nature* **2018**, *556*, 103–107.
[2] J. M. A. Blair, M. A. Webber, A. J. Baylay, D. O. Ogbolu, L. J. V. Piddock, *Nat. Rev. Microbiol.* **2015**, *13*, 42–51.
[3] S. Cheeseman, A. J. Christofferson, R. Kariuki, D. Cozzolino, T. Daeneke, R. J. Crawford, V. K. Truong, J. Chapman, A. Elbourne, *Adv. Sci.* **2020**, *7*, 1902913.
[4] M. Liang, F. Wang, M. Liu, J. Yu, Y. Si, B. Ding, *Adv. Fiber Mater.* **2019**, *1*, 126–136.
[5] X. Fan, F. Yang, J. Huang, Y. Yang, C. Nie, W. Zhao, L. Ma, C. Cheng, C. Zhao, R. Haag, *Nano Lett.* **2019**, *19*, 5885–5896.
[6] Y. Wang, Y. Yang, Y. Shi, H. Song, C. Yu, *Adv. Mater.* **2020**, *32*, 1904106.
[7] M. Zhang, W. Wang, F. Wu, K. Graveran, J. Zhang, C. Wu, *Chem. Eur. J.* **2018**, *24*, 12890–12901.
[8] T. Shi, X. Hou, S. Guo, L. Zhang, C. Wei, T. Peng, X. Hu, *Nat. Commun.* **2021**, *12*, 493.
[9] M. Zhang, F. Wu, W. Wang, J. Shen, N. Zhou, C. Wu, *Chem. Mater.* **2019**, *31*, 1847–1859.
[10] X. Fan, F. Yang, C. Nie, L. Ma, C. Cheng, R. Haag, *Adv. Mater.* **2021**, *33*, 2100637.
[11] B. Yang, Y. Chen, J. Shi, *Chem. Rev.* **2019**, *119*, 4881–4985.
[12] Z. Wei, Y. Zhang, L. Wang, Z. Wang, S. Chen, J. Bao, Y. Xie, B. Su, C. Zhao, *ACS Appl. Mater. Interfaces* **2021**, *13*, 32316–32331.
[13] Y. Yang, X. Wu, L. Ma, C. He, S. Cao, Y. Long, J. Huang, R. D. Rodriguez, C. Cheng, C. Zhao, *Adv. Mater.* **2021**, *33*, 2005477.
[14] L. Ma, F. Jiang, X. Fan, L. Wang, C. He, M. Zhou, S. Li, H. Luo, C. Cheng, L. Qiu, *Adv. Mater.* **2020**, *32*, 2003065.
[15] L. Li, L. Cao, X. Xiang, X. Wu, M. Lang, F. Chen, S. Cao, C. Cheng, D. Deng, L. Qiu, *Adv. Funct. Mater.* **2021**, *31*, 2107530.
[16] Y. Zhang, P. Sun, L. Zhang, Z. Wang, F. Wang, K. Dong, Z. Liu, J. Ren, X. Qu, *Adv. Funct. Mater.* **2019**, *29*, 1808594.
[17] Z. Yuan, C. Lin, Y. He, B. Tao, M. Chen, J. Zhang, P. Liu, K. Cai, *ACS Nano* **2020**, *14*, 3546–3562.
[18] G. Guo, H. Zhang, H. Shen, C. Zhu, R. He, J. Tang, Y. Wang, X. Jiang, J. Wang, W. Bu, *ACS Nano* **2020**, *14*, 13391–13405.
[19] Z. Chen, Z. Wang, J. Ren, X. Qu, *Acc. Chem. Res.* **2018**, *51*, 789–799.
[20] Y. Sang, W. Li, H. Liu, L. Zhang, H. Wang, Z. Liu, J. Ren, X. Qu, *Adv. Funct. Mater.* **2019**, *29*, 1900518.
[21] S. Peng, X. Han, L. Li, S. Chou, D. Ji, H. Huang, Y. Du, J. Liu, S. Ramakrishna, *Adv. Energy Mater.* **2018**, *8*, 1800612.
[22] Z.-Z. Wu, F.-Y. Gao, M.-R. Gao, *Energy Environ. Sci.* **2021**, *14*, 1121.
[23] M. Risch, F. Ringleb, M. Kohlhoff, P. Bogdanoff, P. Chernev, I. Zaharieva, H. Dau, *Energy Environ. Sci.* **2015**, *8*, 661–674.
[24] Q. Zhang, N. M. Bedford, J. Pan, X. Lu, R. Amal, *Adv. Energy Mater.* **2019**, *9*, 1901312.
[25] Z. Wang, Z. Lin, J. Deng, S. Shen, F. Meng, J. Zhang, Q. Zhang, W. Zhong, L. Gu, *Adv. Energy Mater.* **2021**, *11*, 2003023.
[26] Z. Chen, Y. Song, J. Cai, X. Zheng, D. Han, Y. Wu, Y. Zang, S. Niu, Y. Liu, J. Zhu, *Angew. Chem. Int. Ed.* **2018**, *57*, 5076–5080; *Angew. Chem.* **2018**, *130*, 5170–5174.
[27] Z. Chen, Y. Liu, C. Liu, J. Zhang, Y. Chen, W. Hu, Y. Deng, *Small* **2020**, *16*, 1904964.
[28] J. Shan, K. Yang, W. Xiu, Q. Qiu, S. Dai, L. Yuwen, L. Weng, Z. Teng, L. Wang, *Small* **2020**, *16*, 2001099.
[29] S. Li, L. Shang, B. Xu, S. Wang, K. Gu, Q. Wu, Y. Sun, Q. Zhang, H. Yang, F. Zhang, *Angew. Chem. Int. Ed.* **2019**, *58*, 12624–12631; *Angew. Chem.* **2019**, *131*, 12754–12761.
[30] L. Gao, J. Zhuang, L. Nie, J. Zhang, Y. Zhang, N. Gu, T. Wang, J. Feng, D. Yang, S. Perrett, *Nat. Nanotechnol.* **2007**, *2*, 577–583.
[31] Y. Hu, X. Gao, Y. Zhu, F. Muhammad, S. Tan, W. Cao, S. Lin, Z. Jin, X. Gao, H. Wei, *Chem. Mater.* **2018**, *30*, 6431–6439.
[32] W. Shao, C. He, M. Zhou, C. Yang, Y. Gao, S. Li, L. Ma, L. Qiu, C. Cheng, C. Zhao, *J. Mater. Chem. A* **2020**, *8*, 3168–3179.
[33] S. Saraswati, S. M. Marrow, L. A. Watch, P. P. Young, *Nat. Commun.* **2019**, *10*, 3027.

Manuscript received: October 12, 2021
Accepted manuscript online: November 26, 2021
Version of record online: January 3, 2022